Three-dimensional radial anisotropic structure of the North American upper mantle from inversion of surface waveform data

Federica Marone,[1,*] Yuancheng Gung[2] and Barbara Romanowicz[1]

[1]*Berkeley Seismological Laboratory, University of California,* 215 *McCone Hall #4760, Berkeley,* CA 94720-4760*, USA.*
E-mail: federica@seismo.berkeley.edu
[2]*Department of Geosciences, National Taiwan University, Taipei, Taiwan*

SUMMARY

Seismic anisotropy provides insight into palaeo and recent deformation processes and, therefore, mantle dynamics. In a first step towards a model for the North American upper mantle with anisotropy characterized by a symmetry axis of arbitrary orientation, aimed at filling the gap between global tomography and *SKS* splitting studies, we inverted long period waveform data simultaneously for perturbations in the isotropic *S*-velocity structure and the anisotropic parameter $\xi = \frac{v_{SH}^2}{v_{SV}^2}$, in the framework of normal mode asymptotic coupling theory (NACT). The resulting 2-D broad-band sensitivity kernels allow us to exploit the information contained in long period seismograms for fundamental and higher mode surface waves at the same time. To ensure high quality of the retrieved regional upper-mantle structure, accurate crustal corrections are essential. Here, we follow an approach which goes beyond the linear perturbation approximation and split the correction into a linear and non-linear part. The inverted data set consists of more than 40 000 high quality three component fundamental and overtone surface waveforms, recorded at broad-band seismic stations in North America from teleseismic events and provides a fairly homogeneous path and azimuthal coverage. The isotropic part of our tomographic model shares the large-scale features of previous regional studies for North America. We confirm the pronounced difference in the isotropic velocity structure between the western active tectonic region and the central/eastern stable shield, as well as the presence of subducted material (Juan de Fuca and Farallon Plate) at transition zone depths. The new regional 3-D radial anisotropic model indicates the presence of two distinct anisotropic layers beneath the cratonic part of the North American continent: a deep asthenospheric layer, consistent with present day mantle flow, and a shallower lithospheric layer, possibly a record of ancient tectonic events.

Key words: broadband, seismic anisotropy, surface waves, tomography, upper mantle, waveform analysis.

1 INTRODUCTION

In the early 1960s, theoretical work (e.g. Anderson 1961) on the dispersive properties of transversely isotropic media suggested that radial anisotropy in the upper mantle could have a pronounced effect on the shape of surface wave dispersion curves and could lead to an apparent discrepancy between Love and Rayleigh wave data. The incompatibility of dispersion curves measured for Love and Rayleigh waves observed by Aki & Kaminuma (1963) in Japan and McEvilly (1964) in the central US indeed provided the first evi-

dence for the radial anisotropic structure of the upper mantle. This evidence eventually led to the construction of a global 1-D reference Earth model with 2–4 per cent polarization anisotropy in the mantle down to 220 km depth (Dziewonski & Anderson 1981). With the advent of the first long-period digital seismographs in the late 1970s (Global Digital Seismic Network), the widespread character of radial anisotropy was confirmed. Nataf *et al.* (1984, 1986) first mapped the global 3-D variations of radial anisotropy in the upper mantle by simultaneously inverting fundamental mode dispersion curves for Rayleigh and Love waves. Lévêque & Cara (1983, 1985) and Cara & Lévêque (1988) included higher mode data to investigate the upper-mantle radial anisotropic structure of the Pacific Ocean and North America. Increased details in the global distribution of transverse isotropy have recently been imaged by Ekström & Dziewonski (1998) using global Love and Rayleigh wave

dispersion measurements in the period range 35–300 s, in addition to long period waveform and traveltime data. Nowadays the presence of radial anisotropy has been reported both at regional and global scales, from the subcrustal lithosphere and asthenosphere (e.g. Montagner & Jobert 1988; Montagner & Tanimoto 1991; Debayle & Kennett 2000), down to the core mantle boundary (e.g. Panning & Romanowicz 2004).

Seismic anisotropy can be explained by different structural arrangements, both at the micro and macroscopic scale. In the upper mantle, it is usually attributed to lattice preferred orientation (LPO) of anisotropic minerals such as olivine and pyroxene (e.g. Estey & Douglas 1986), with mineral re-orientation occurring for instance during deformation processes or in the presence of a mantle flow.

Seismic anisotropy has a first-order effect and can be responsible for a significant part of the inferred 3-D variations in seismic velocities in tomographic studies. Seismic data that are interpreted using isotropic theories can lead to incorrect conclusions about mantle structure. For example, isotropic global S-velocity (v_{SH}, v_{SV} or hybrid) models differ significantly in the depth range 200–400 km. However, this apparent disagreement between tomographic models derived using different types of data (e.g. Rayleigh versus Love data) can be reconciled when anisotropy is taken into account (Gung *et al.* 2003).

Seismic anisotropy is not only required to correctly interpret tomographic models but, since its presence is strictly related to deformation processes, the detailed knowledge of the seismic anisotropic structure of the Earth's mantle can provide a wealth of new information on past and present mantle dynamics. In spite of its enormous potential to shed light onto the deformation of the Earth's interior, this powerful tool has been until recently underexploited, especially at the continental scale.

The North American continent, featuring the juxtaposition of Phanerozoic belts against one of the largest Precambrian shields on Earth, is the ideal target for the investigation of the structure and dynamics of the continental upper mantle by means of high resolution 3-D tomographic models of the isotropic and anisotropic mantle structure. In particular, timely geophysical questions such as the relation to geological age of the variations in thickness of the continental lithosphere, the relation of upper-mantle anisotropy to present day asthenospheric flow and/or past tectonic events, the nature and strength of the lithosphere/asthenosphere coupling and the driving mechanisms of plate motions can be explored.

1.1 Tectonic background

The geology and tectonics of the North American continent divide its landmass into two distinct provinces: the tectonically active western region and the stable central and eastern shields, with the boundary almost perfectly coincident with the Rocky Mountain Front. The recent evolution of western North America has been controlled by the Mesozoic–Cenozoic ocean–continent collisional system. Eastward flat subduction of oceanic lithosphere (75–40 Ma) is thought to be responsible for the Laramide orogeny, characterized by minor horizontal shortening in the crust, but considerable crustal thickening (up to 55 km), explained by eastward transfer of ductile lower crustal material (Bird 1988). This thickened crust now isostatically supports the high elevation observed in the Rocky Mountains region. About 40 Ma ago, the ongoing flat subduction experienced slab steepening and was gradually replaced by a transform system, giving rise to a growing slab window (Dickinson & Snyder 1979). As a consequence, the base of the crust over a vast region west of the

Rockies was exposed to upwelling hot asthenosphere. Crustal extension in the Basin and Range province followed, triggered by decreased crustal strength induced by higher temperatures and increased gravitational forces arising from higher elevation, a consequence of isostatic rebound (Bird 1988). Currently, tectonic activity, which manifests itself in a wide variety of phenomena and deformation mechanisms, is still observed throughout the western part of the continent. In fact, western North America is characterized by a complex plate boundary featuring most deformation styles possibly present at such margins: subduction of the Pacific Plate in the North and of the young Juan de Fuca plate offshore the western US-Canadian border, strike-slip along the Queen Charlotte–Fairweather system in Canada and along the San Andreas fault in California, extension in Baja California. Moreover, in addition to the recorded seismicity, there is evidence for recent tectonic activity such as, for example, Yellowstone volcanism and Holocene volcanism documented throughout the Cascadian Range, a region still experiencing ongoing continental arc volcanism. The interior of the North American continent mainly consists of the Precambrian Continental Platform and the Canadian Shield, tectonic provinces which have been stable since 1 Ga (Grenville orogeny and Midcontinent Rift formation), with few Archean cores (e.g. the Superior province), which experienced the last deformation 2.7 Ga ago. The last tectonic activity in the eastern part of North America dates back to the Palaeozoic and is related to the Appalachian orogeny (450–350 Ma).

1.2 Previous studies

Knowledge of the shear wave anisotropic structure of the North American upper-mantle results mainly from global tomographic models and *SKS* splitting studies. Traditionally, best results in mapping upper-mantle radial and azimuthal anisotropy at the global scale have been achieved using fundamental mode surface waves (e.g. Tanimoto & Anderson 1984; Montagner & Tanimoto 1991). Inclusion of overtones in the development of recent global tomographic models (Gung *et al.* 2003; Panning & Romanowicz 2006) significantly improves the resolution at depth. Such models show for instance radial anisotropy with $v_{SH} > v_{SV}$ in the depth range 200–400 km beneath continental cratons, such as the Canadian shield, suggesting horizontal shear in the sublithospheric asthenosphere. Although during the last years increasing refinement in global 3-D tomographic models has been achieved, existing anisotropic models still have insufficient resolution to image structures characterized by wavelengths smaller than 1000 km. Most regional studies of North America have focused on the analysis of Rayleigh wave dispersion (Alsina *et al.* 1996; Godey *et al.* 2003) or waveform data (Van der Lee & Nolet 1997a; Frederiksen *et al.* 2001; Van der Lee 2002) in the framework of elastic isotropy, with recent efforts to also map azimuthal anisotropy (Li *et al.* 2003, 2005). Azimuthal anisotropy in the North American upper mantle has been extensively studied using shear wave splitting measurements, abundantly performed on *SKS* phases (e.g. Silver & Chan 1988; Savage *et al.* 1990; Vinnik *et al.* 1992; Savage & Silver 1993; Silver & Kaneshima 1993; Bostock & Cassidy 1995; Liu *et al.* 1995; Özalaybey & Savage 1995; Savage *et al.* 1996; Barruol *et al.* 1997; Kay *et al.* 1999; Levin *et al.* 1999; Fouch *et al.* 2000; Savage & Sheehan 2000). Models derived with this approach are characterized by the horizontal resolution required by regional studies and show for instance rapid variations of the fast axis direction of anisotropy in the western US. However, such measurements do not provide any constraints on the depth of the anisotropic layer and strong

trade-offs between the strength of anisotropy and the thickness of the anisotropic layer exist. Because of these trade-offs, shear wave splitting analysis alone is not suitable to test hypotheses regarding the depth and origin of the observed anisotropy and to address questions about the relation of upper-mantle anisotropy to present day asthenospheric flow and/or past tectonic events, even less in the central and eastern US, where the fast axis direction of anisotropy inferred from shear wave splitting is very similar under both hypotheses. In a recent study of the eastern North American upper mantle, Gaherty (2004) combines constraints derived from surface waves and splitting measurements and suggests the presence of two layers of anisotropy, a lithospheric and an asthenospheric layer, as previously proposed for other cratonic areas (e.g. Debayle *et al.* 2005).

Here we aim at closing the gap between global anisotropic tomographic models and point measurements provided by *SKS* splitting studies. We present the first 3-D radially anisotropic model for the upper-mantle anisotropic structure beneath the North American continent derived from long period fundamental and higher modes surface waveform data, and characterized by the appropriate horizontal and vertical resolution to gain a better understanding of the lateral and depth distribution of anisotropy in a continental setting. The analysis of azimuthal anisotropy is addressed in a companion paper (Marone & Romanowicz 2007b).

2 METHODOLOGY

We apply a full waveform tomographic method based on the non-linear asymptotic coupling theory (NACT, Li & Romanowicz 1995), which permits the inversion of entire long period seismograms in the time domain (including fundamental mode, overtones and body wave portions of the record) for 3-D elastic structure. NACT is a normal-mode perturbation approach, which takes into account coupling between modes both along and across dispersion branches. The asymptotic calculation of this coupling allows the computation of 2-D broad-band sensitivity kernels which more rigorously reproduce the sensitivity of body waveforms to structure along and around the ray geometrical path in the vertical plane containing the source and the receiver. This body wave character of the 2-D kernels is also important to accurately model the waveforms of surface wave overtones. In contrast, traditional methods, based on path average approximation and infinite frequency 'ray theory', rely on 1-D sensitivity kernels, an assumption which is strictly valid only for fundamental mode surface waves. We do not consider off great circle path sensitivity in the horizontal direction, which gives rise to focusing/defocusing effects (e.g. Zhou *et al.* 2005). These effects are important for amplitude fitting. Here, we are, however, primarily concerned with fitting the phase and for that, the 2-D effects in the vertical plane are dominant, especially for overtones. The dominance of 2-D effects in the vertical plane can be assessed by considering an asymptotic expansion of normal mode first order perturbation theory, which shows that 2-D coupling effects in the vertical plane are of zeroth order, while focusing effects are of higher order (e.g. Romanowicz 1987; Li & Romanowicz 1995; Romanowicz *et al.* 2007).

A transversely isotropic medium with a vertical axis of symmetry is described by density ρ and the five Love coefficients (A, C, F, L and N) (Love 1927). Equivalently, we initially parametrize our model in terms of ρ, the Voigt average isotropic *P*- and *S*-velocities (v_S and v_P), and the anisotropic parameters $\xi = N/L$, $\phi = C/A$ and $\eta = F/(A - 2L)$. To reduce the number of parameters in the

inversion and keep only those that are best resolved by our surface wave data set (v_S and ξ), we assume empirical scaling relations as inferred from laboratory experiments ($\frac{\delta \ln v_P}{\delta \ln v_S} = 0.5$; $\frac{\delta \ln \rho}{\delta \ln v_S} = 0.33$; $\frac{\delta \ln \eta}{\delta \ln \xi} = -2.5$; $\frac{\delta \ln \phi}{\delta \ln \xi} = -1.5$; Montagner & Anderson 1989). We opted for this particular parametrization in terms of v_S and ξ instead of the more traditional approach which solves for v_{SV} and v_{SH}, to avoid additional uncertainties on the amplitude and possibly even sign of the anisotropic parameter ξ introduced by damping in the inversion process. Indeed, if ξ is computed after the inversion from the derived v_{SV} and v_{SH}, its value can be biased by the different effect of damping on the two velocity parameters. We compute appropriate 2-D sensitivity kernels for weak transverse isotropy (Panning & Romanowicz 2006). These anisotropic kernels ensure high resolution at depth, not guaranteed by the use of simplified theoretical assumptions such as isotropic sensitivity kernels, which ignore the influence of radial anisotropy on depth sensitivity kernels (e.g. Gung *et al.* 2003).

We solve the inversion problem iteratively using a least-squares approach (Tarantola & Valette 1982) and update the partial derivatives after each iteration. We apply regularization through *a priori* data and model matrices. In particular, we scale each equation according to individual weighting values, which take into account noise, waveform amplitude and path redundancy (Li & Romanowicz 1996) and we damp the model norm towards our reference model PREM (Dziewonski & Anderson 1981). Such a choice ensures that in regions not constrained by the data, the resulting model is very close to PREM and no artificial anomalies are introduced. We also investigated roughness damping. Although we varied the damping parameters over a broad range, we hardly noticed any difference in the resulting model, most likely due to the smoothing character of the basis functions used. We therefore decided that roughness damping was not necessary in our inversion. As starting model we use a global 3-D anisotropic model (Panning & Romanowicz 2006). The solution to the inverse problem is very stable. After the first iteration, where the largest changes are observed, the modifications in the solution are small. Our preferred model has been obtained after four iterations.

In theory, the retrieved radial anisotropic model could be biased by the presence of azimuthal anisotropy, neglected at the present stage of this study. In practice, with sufficient azimuthal coverage, this possible effect is reduced because the azimuthal variations will be averaged out at each point of the model. This study, limited to radial anisotropy, should be regarded as a first step towards a more complex model of anisotropy, where the assumption of a vertical symmetry axis will be dropped and which will, therefore, still be characterized by radial anisotropy but with a symmetry axis with an arbitrary orientation (e.g. Montagner & Nataf 1988). Such an anisotropic model will be able to describe both radial and azimuthal anisotropic observations.

2.1 Model parametrization

The NACT algorithm has until now been applied only at the global scale, with lateral parametrization in terms of spherical harmonics (e.g. Gung *et al.* 2003). Similarly to previous studies (e.g Wang *et al.* 1998; Boschi *et al.* 2004), we have adapted the procedure to the regional case by implementing a lateral parametrization in terms of spherical splines on a triangular grid of knots (Wang & Dahlen 1995).

In particular, we use a spherical tesselation method to partition the Earth's surface into approximately equilateral triangles, whose

(a)

(b)
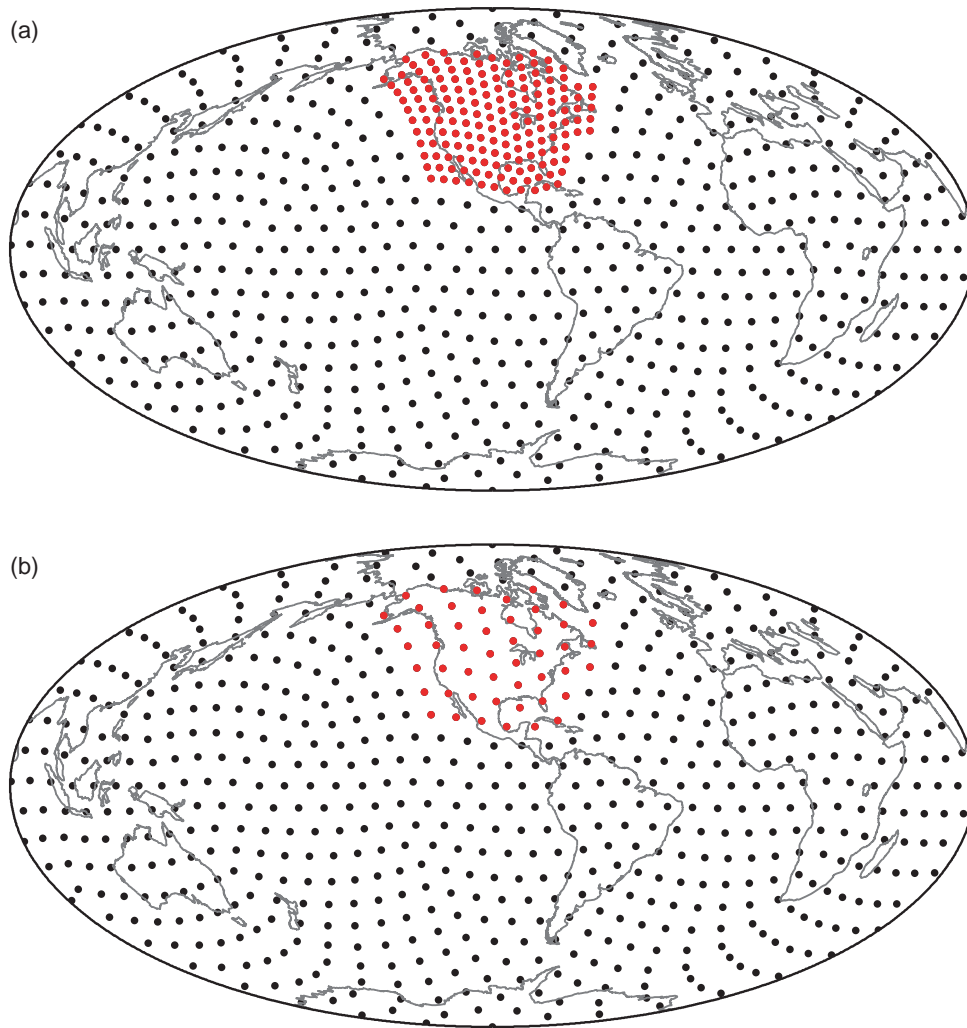
Figure 1. Triangular grid of knots used in the inversion—(a) For the parametrization of the isotropic S-velocity structure v_S, (b) For the parametrization of the anisotropic parameter ξ. The red dots mark the target region and represent the subset of model parameters which are being perturbed. The finer and coarser parametrizations are equivalent to a spherical harmonics expansion of about degree 46 and 24, respectively (average knot spacing of 3.95° and 7.9°).

vertices form a triangular grid of knots. For high resolution regional tomographic studies, the mesh for the target region can be refined by adding knots halfway between two neighbouring grid points, until the desired knot spacing has been reached, while maintaining a coarser mesh throughout the rest of the globe (Fig. 1). This approach allows flexibility: the grid spacing can, for instance, be chosen as a function of the inhomogeneous data coverage, and therefore, achieve maximum resolution in the ideally sampled region, without need for overparametrizing the areas with insufficient data density. In addition, in multiparameter studies (e.g. simultaneous inversion for v_S and ξ), large variability in the expected resolution between different parameters could exist. In such a case, a parameter-specific parametrization is highly desirable (Fig. 1).

We have implemented a lateral parametrization in terms of spherical splines on this irregular triangular grid of knots. We define a set of spherical spline basis functions in terms of the geodesic distance Δ to a knot. The normalized spherical spline function centred upon a knot is given by Lancaster & Salkauskas (1986):

$$f(\Delta) = \begin{cases} \frac{3}{4}\bar{\Delta}^{-3}\Delta^3 - \frac{6}{4}\bar{\Delta}^{-2}\Delta^2 + 1, & \Delta \leq \bar{\Delta} \\ -\frac{1}{4}\bar{\Delta}_1^3 + \frac{3}{4}\bar{\Delta}_1^2 - \frac{3}{4}\bar{\Delta}_1 + \frac{1}{4}, & \bar{\Delta} \leq \Delta \leq 2\bar{\Delta}, \end{cases}$$

where $\bar{\Delta}$ is the average epicentral distance between neighbouring knots, $\Delta_1 = \Delta - \bar{\Delta}$, and $\bar{\Delta}_1 = \Delta_1/\bar{\Delta}$. Vertically the model is parametrized in terms of cubic splines (Mégnin & Romanowicz 2000), with a finer knot spacing in the upper mantle, to reflect the data sampling with depth.

In addition to the high flexibility allowed by this approach in the design of the mesh, an additional advantage over global types of parametrizations such as spherical harmonics, is that it permits the perturbation of only a subset of the model parameters, for instance the ones falling within the target area, while using the entire set to correct the data for the heterogeneous structure outside the study region. Here, only the model parameters located in North America (in red in Fig. 1) are perturbed, while the data are corrected for the global 3-D heterogeneous structure outside of the target region using our 3-D global radial anisotropic starting model (Panning & Romanowicz 2006). Because the mantle structure inside the study region is constrained by a good path and azimuthal coverage (Figs 2 and 3) at each sampling point, the effect of inaccurate 3-D structure outside the target region should be minimal on the obtained model, because any arising inconsistency would be mapped into the null space of the inversion.

## Vertical component   Transverse component
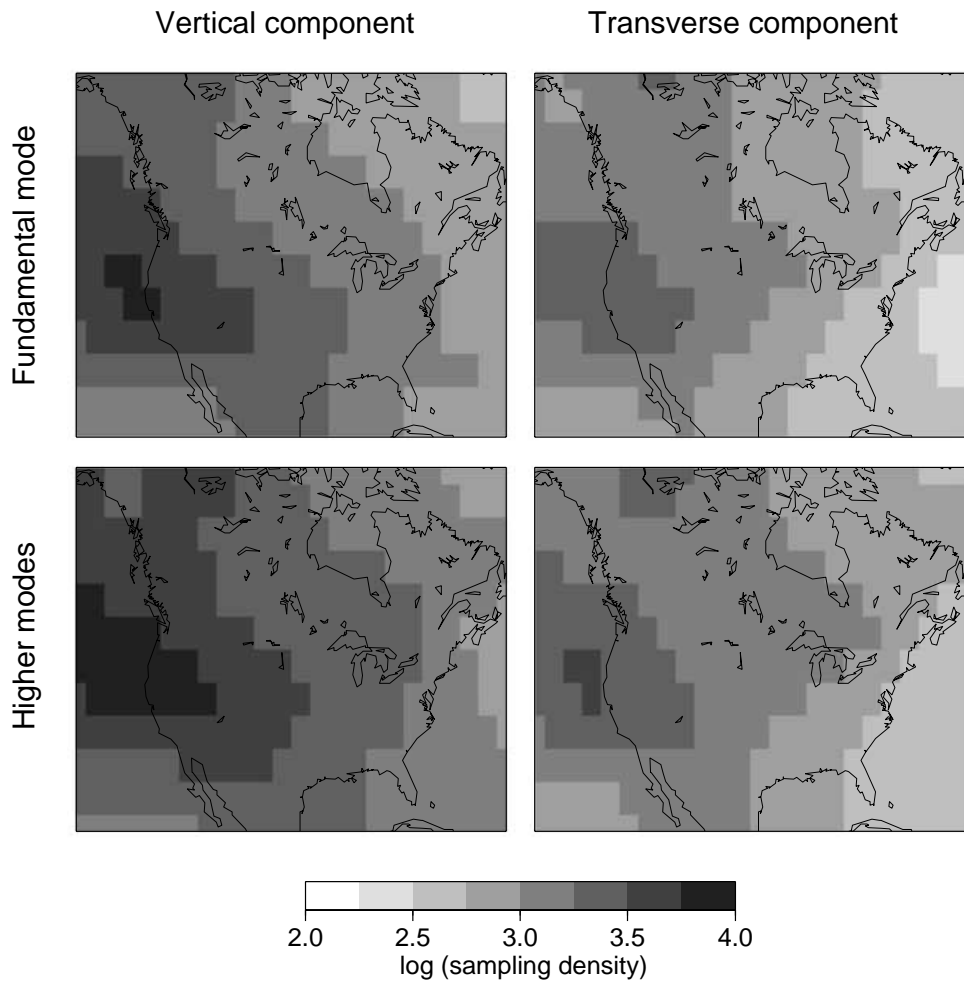
Figure 2. Path coverage provided by minor arc source-station paths for fundamental (top) and higher modes (bottom) waveforms used in this study for the vertical component (left) and the transverse component (right). The region is divided into $5° \times 5°$ elements. The sampling density for each block has been computed as the number of paths crossing it, scaled to take into account the area difference of each element with latitude.
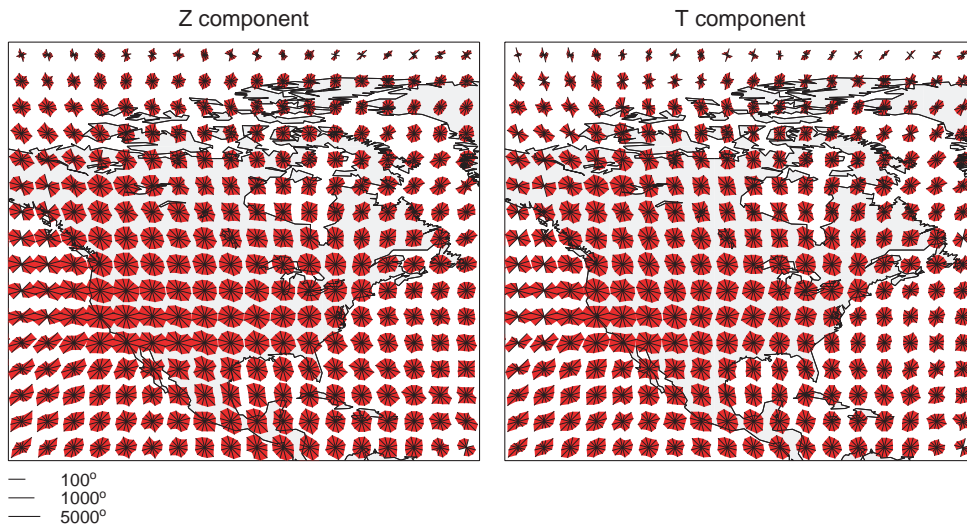
Figure 3. Azimuthal coverage provided by minor arc source-station paths for fundamental and higher-mode waveforms used in this study for the vertical (left) and transverse component (right). The region is divided into $5° \times 5°$ elements and $30°$ wide azimuthal sections. The segment length is proportional to the cumulative path length (in degrees) in the corresponding block and azimuthal range. The scale is logarithmic.
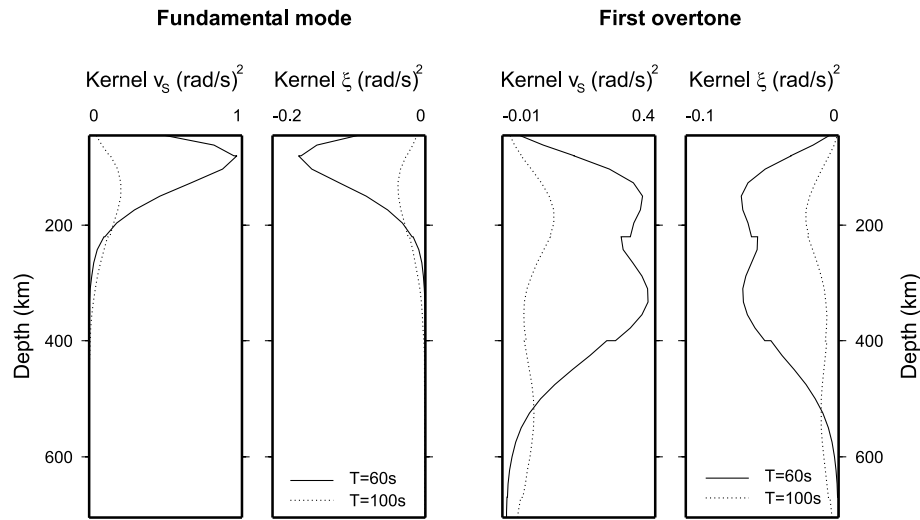
Figure 4. Depth sensitivity kernels for the isotropic *S*-velocity structure and radial anisotropy for the fundamental mode (on the left) and the first overtone (on the right) at periods of 60 s (solid line) and 100 s (dotted line).
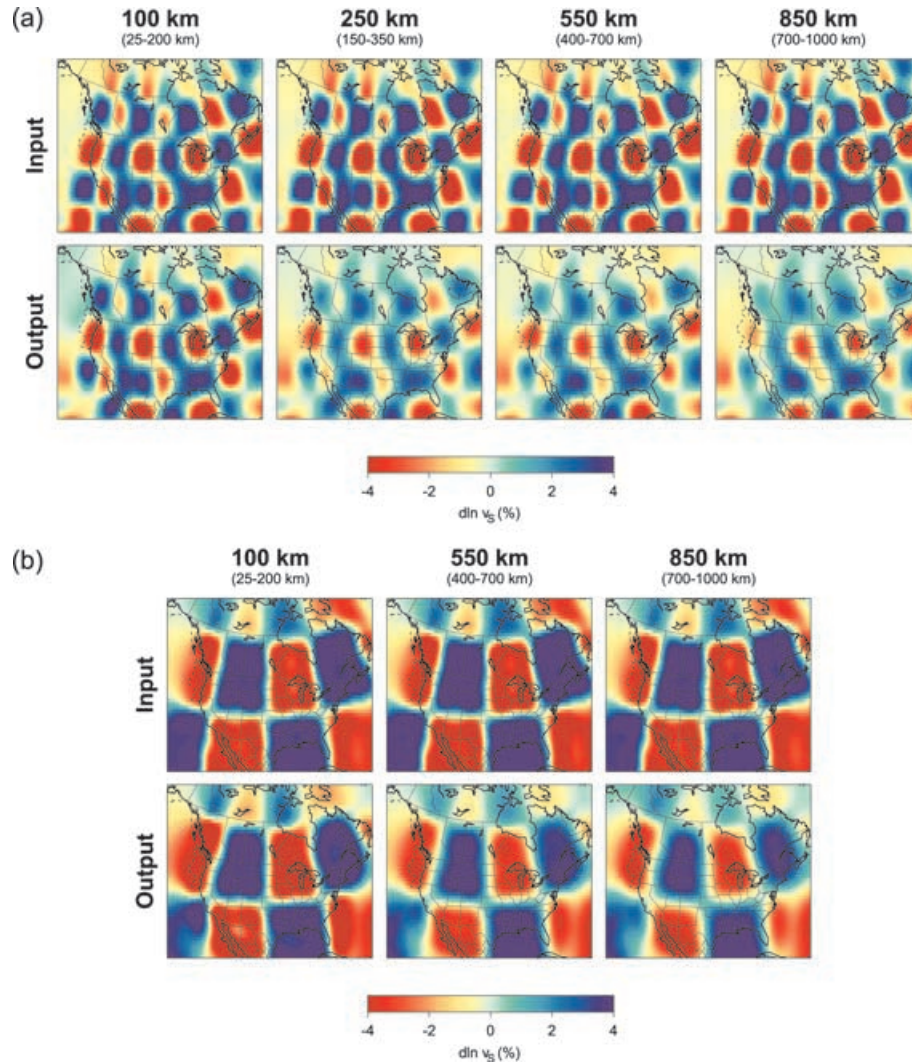
Figure 5. Checkerboard-like resolution test results for the isotropic *S*-velocity structure at different depths (indicated by the bold numbers). The synthetic input models, shown in the top panels, consist of a layer, located at different depths (given by the numbers in brackets) of alternating negative and positive isotropic anomalies of—(a) $10° \times 10°$ and (b) $20° \times 20°$ size. The input pattern is smoother than a rigorous checkerboard pattern as it is developed on the basis of spherical splines which we use in parametrizing our models The recovered isotropic part of the model is shown in the bottom panels.
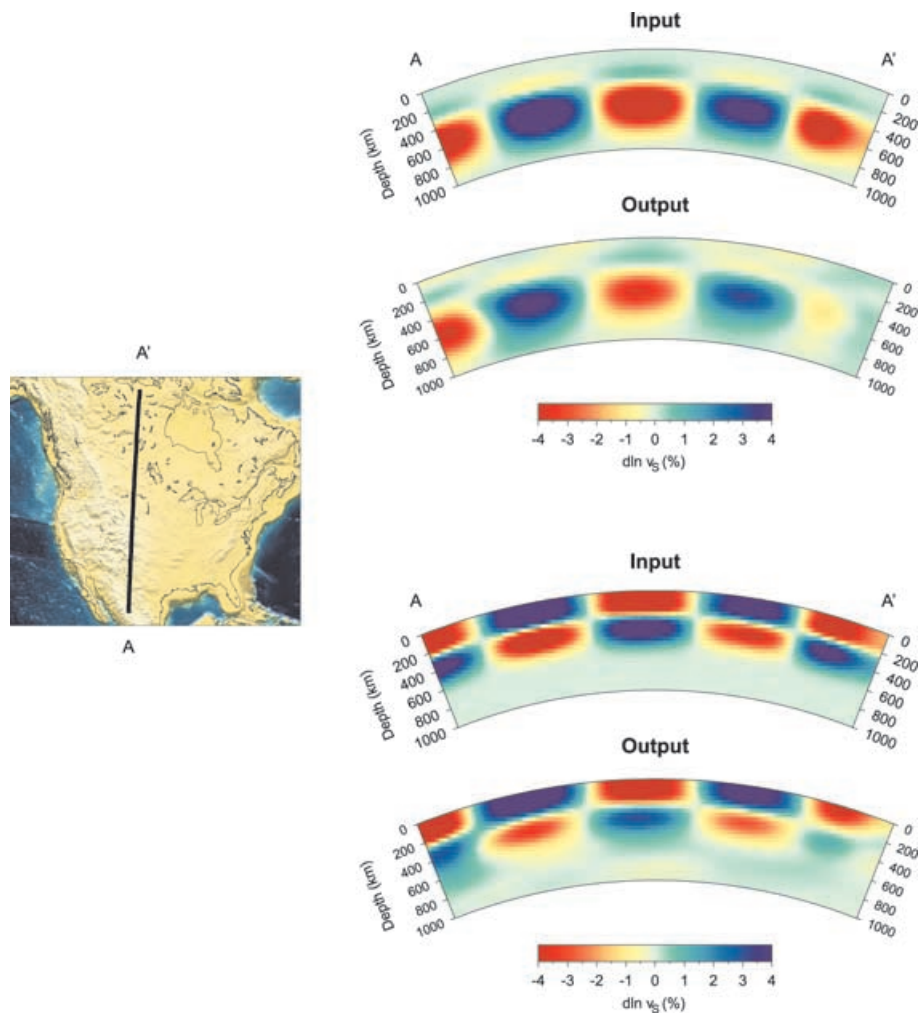
Figure 6. Resolution test results for two synthetic isotropic *S*-velocity structures shown along profile AA′.

2.2 Crustal corrections

Body and surface wave data sets used in mantle seismic tomography are sensitive to crustal structure, but cannot resolve details within the crust. Accurate crustal corrections are, therefore, essential to prevent mapping crustal features into mantle tomographic images and thus biasing the modelled structure. In seismic tomographic studies, the effect of shallow-layer features is often removed from the data by assuming an *a priori* crustal model and applying linear perturbation corrections. However, lateral variations in Moho depth can be fairly large even over short distances, as for instance at ocean/continent transitions and the adequacy of linear corrections is questionable. In fact, Montagner & Jobert (1988) showed that the non-linearity of shallow-layer corrections is often not negligible even at long periods. In high resolution upper-mantle regional tomographic studies, it is therefore important to take the crustal structure into account in a more accurate way (e.g. Van der Lee & Nolet 1997a; Boschi & Ekström 2002).

In the present study, and as described in detail in Marone & Romanowicz (2007a), we follow the approach originally proposed by Montagner & Jobert (1988) for fundamental mode Rayleigh and Love wave phase velocity measurements, where the shallow layer correction is decomposed into a linear and a non-linear part. As in traditional approaches, we assume an *a priori* 3-D crustal model (e.g. Woodhouse & Dziewonski 1984). Differently from traditional procedures, for the shallow layer correction we do not use, throughout the study region, the same 1-D sensitivity kernels computed for the global 1-D reference model (e.g. PREM). We define instead a set of different 1-D sensitivity kernels according to the local crustal structure (e.g. ocean, shield and orogen).

Our 3-D *a priori* crustal model for the shallow layers corrections is the crustal structure used to derive our 3-D global anisotropic starting model and consists of two discontinuities: the Earth's topography and Moho interface. The Earth's topography is modelled according to ETOPO-5 (National Geophysical Data Center 1988), the Moho interface according to CRUST2.0 (Bassin *et al.* 2000). Since the data sensitivity to the topography of discontinuities is significantly larger than to the 3-D heterogeneous elastic crustal structure, we only consider and correct for variations in the two above-mentioned discontinuities. For the elastic velocity structure in the crust, the 1-D PREM model throughout the study region is assumed.

3 DATA

In this study, we consider fundamental and overtone surface waveforms selected from three component long period seismograms. Surface wave data for paths relevant to the study region have been extracted from the existing compilation used for global tomography in Panning & Romanowicz (2006). This data set has been
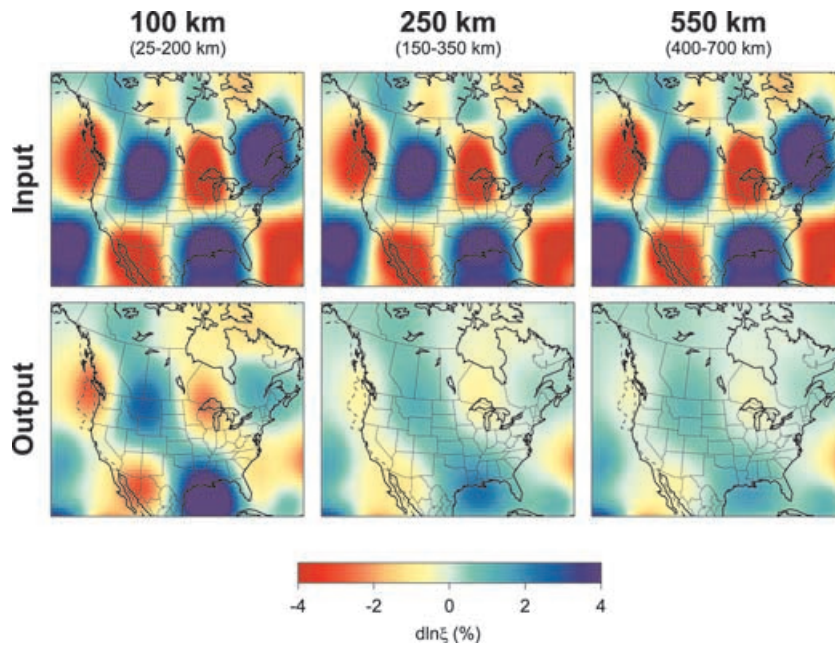
Figure 7. Checkerboard-like resolution test results for the radial anisotropic structure at different depths (indicated by the bold numbers). The synthetic input models, shown in the top panels, consist of a layer, located at different depths (given by the numbers in brackets) of alternating negative and positive anomalies of $20° \times 20°$ size. The recovered ξ model is shown in the bottom panels.

further complemented with waveforms from events at teleseismic and far regional distances ($15° < \Delta < 165°$) recorded at broadband seismic stations in North America. In this region, numerous permanent broad-band stations have been operational for at least several years, as part of the global seismic network (IRIS), the US National Seismic Network (USNSN), the Canadian Regional Seismic Network (CRSN), as well as regional broad-band networks, such as the BDSN and Terrascope in California. Data recorded during temporary broad-band experiments (MOMA (Wysession *et al.* 1996), ABITIBI, FLED, CDROM and RISTRA (Wilson *et al.* 2002, 2003)) have also been included. The collected data set includes data for 657 events from 1990 to 2003, with M_W between 6.0 and 7.0. The main criteria guiding the event selection has been the achievement of the best possible path and azimuthal coverage for the North American continent (Figs 2 and 3).

From each deconvolved and filtered (between 60 and 400 s) three component seismogram, individual fundamental and higher mode first orbit energy packets have been extracted using an automated picking algorithm (Panning & Romanowicz 2006) based on the comparison of the observed trace with the corresponding synthetic seismogram computed in the reference model PREM (Dziewonski & Anderson 1981), using a number of criteria including correlation and rms difference. To ensure a high quality data set, we additionally opted for a visual inspection of each trace, so that noisy data are readily rejected as well as records affected by timing errors, errors in instrument corrections, unmodelled source effects and near-receiver structure. The applied windowing scheme characterized by the selection of distinct wavepackets allows flexibility in assigning appropriate weights to different phases so as to enhance, for instance, the contribution of higher modes with respect to the naturally dominating fundamental mode. In particular, the individual weighting values used in our inversion, in addition to waveform amplitude, also take into account noise and path redundancy (Li & Romanowicz 1996).

Our final data set consists of more than 18 000 fundamental mode and 27 000 higher modes high quality surface wavepackets. We ex-

pect that the achieved fairly homogeneous path and azimuthal coverage for North America (Figs 2 and 3) will be further improved in the future, by taking advantage of the broad-band data set that is being collected under the USArray effort within EarthScope.
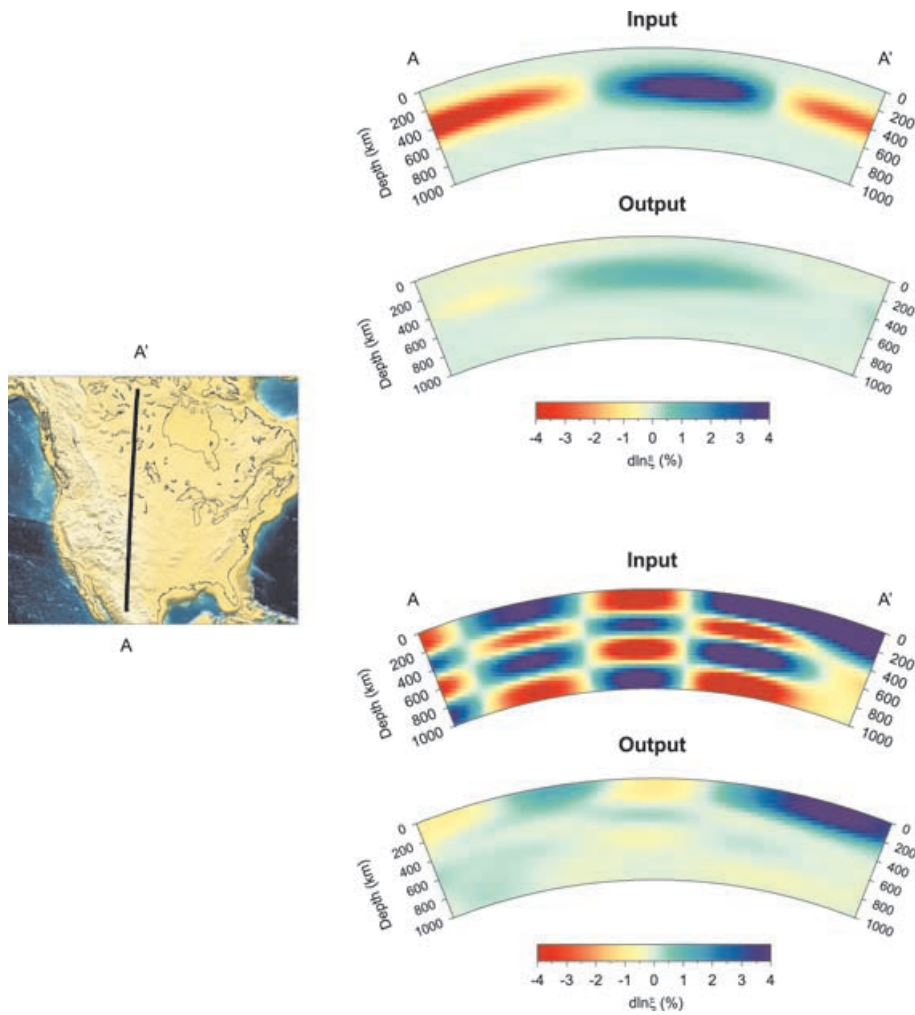
4 RESOLUTION

A first idea of the resolution power of our data set can be gained from inspection of 1-D depth sensitivity kernels (Fig. 4). Waveform sensitivity to the isotropic *S*-velocity structure is about five times larger than to radial anisotropy, both for the fundamental mode and the overtones. As a consequence, we expect better resolution for the isotropic than for the anisotropic structure, a factor that has led us to the choice of a different horizontal mesh for these two parameters (Fig. 1). The chosen grid and the smoothing inherent in the basis functions used (spherical splines) dictate the minimum horizontal size of resolved features: about 700 and 1500 km for isotropic *S*-velocity and radial anisotropic anomalies, respectively.

The resolution of tomographic models derived in least-squares inversions is commonly assessed through synthetic tests using the model resolution matrix (e.g. Menke 1989). Although such an approach was originally developed for linear problems, it remains a good approximation for mildly non linear problems (Tarantola 2004), solved iteratively as in this study. This technique is particularly suitable for addressing the model resolution given the used data set and the applied damping scheme, while it is not informative on uncertainties arising from theoretical approximations inherent in the forward problem or errors in the data not taken into account by the *a priori* data covariance matrix.

To test different aspects of the resolution, a variety of different earth models has been chosen. A series of checkerboard-like tests with synthetic anomalies in v_S or ξ at different depths and of different sizes show that the resolution decreases with depth and larger anomalies are better resolved than smaller ones. Also, the recovered
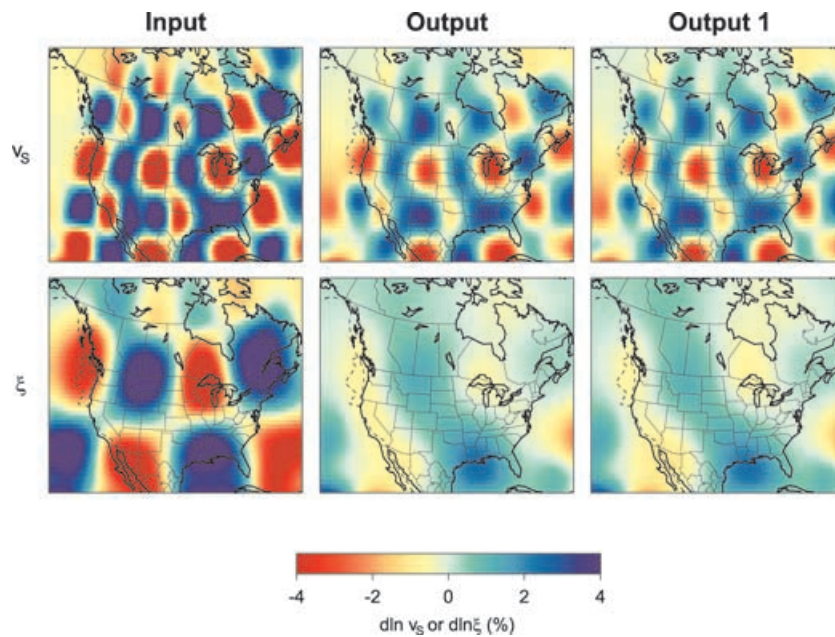
Figure 8. Resolution test results for two synthetic radial anisotropic structures shown along profile AA′.

anomaly amplitude decreases with depth. Examples for the isotropic *S*-velocity structure are shown in Figs 5 and 6. Here the input model is purely isotropic and the anisotropic part is set to 0. Thanks to the inclusion of higher modes (e.g. Fig. 4), good recovery of the input pattern throughout most of the study region is observed down to the top of the lower mantle, both for $10° \times 10°$ and $20° \times 20°$ size anomalies. The amplitude of the anomalies is best recovered in the case of the larger scale pattern. Our data set provides an excellent resolution of the depth extent of isotropic velocity anomalies as well as of the vertical transition from positive to negative anomalies and viceversa (Fig. 6). In Figs 7 and 8, we consider an input model with only lateral variations in ξ. As anticipated, the resolution for ξ is not as good as for the isotropic velocity structure (Fig. 5). The anisotropic anomaly pattern is recovered in the uppermost mantle, but the resolution is degraded with increasing depth, where loss of the restored anomaly amplitudes and horizontal smearing are observed. The resolution of the depth extent of radial anisotropic anomalies is, however, satisfactory throughout the upper mantle (Fig. 8).

The synthetic input models used for the tests presented in Figs 5–8 were characterized by positive and negative anomalies confined to either the isotropic or anisotropic part of the model space, while the remaining model parameters were set to 0. Since the aim of these initial 'standard' checkerboard tests was the investigation of the limits of the resolution of either the isotropic *S*-velocities or the anisotropic

parameter ξ, the output structure, mostly small, corresponding to the part of the input model set to 0, has therefore, not been shown. In contrast, the following series of tests has been designed to investigate trade-offs between the isotropic and anisotropic portion of the model space and demonstrates that contamination is minimal. In a first example (Fig. 9), the synthetic input model consists of horizontally alternating positive and negative anomalies between 150 and 350 km depth in both v_S and ξ. While the anomalous layer is located at the same depth in both the isotropic and anisotropic structure, the wavelength of the anomalies is different in the two cases to facilitate the detection of potential trade-offs. The output model (column labelled 'Output') does not show any evidence of contamination. This conclusion is confirmed by the comparison of the same output model with the results of tests where the synthetic input anomalies are confined to either the isotropic or anisotropic portion of the model (Figs 5–8, the relevant horizontal slices shown again in Fig. 9 in column 'Output 1') and where, therefore, contamination is not possible since the input structure of the part of the model not shown is set to 0. This test clearly shows that when anomalous structure is present in both portions of the model, trade-offs are practically non-existent. A final set of tests is presented in Fig. 10. Here we consider input models with structure only in v_S (Fig. 12a) or in ξ (Fig. 12b) as for the tests presented in Figs 5–8. In this example, we opted however for a synthetic input model characterized by more

Figure 9. Resolution test results for a synthetic input model (left-hand column) consisting of horizontally alternating positive and negative anomalies between 150 and 350 km depth. The anomalous layer is located at the same depth in both the isotropic and anisotropic portion of the model, but the size of the anomalies is different in the two cases. The output model is shown in the middle column ('Output'). The right column ('Output 1') shows the results of tests where the synthetic input anomalies were confined to either the isotropic or anisotropic portion of the model (as in Figs 5 and 7, for *Vs* and ξ, respectively). All horizontal slices are for a depth of 250 km.

realistic anomalies expected for the North American upper-mantle structure than a checkerboard-like pattern. We explore possible contaminations by examining the output structure in the parameter that was set to zero in the input model. The output models confirm that large-scale features in our study are well resolved throughout the upper mantle, although amplitude underestimation is observed at depth, in particular, for the radial anisotropic structure. In addition, the results in Fig. 10(b) show that the isotropic *S*-velocity structure is only marginally contaminated by radial anisotropic features and corroborate the high robustness of this portion of the model. The results for the opposite case (recovery of anisotropic structure, Fig. 10a) are also encouraging, although at depth minor trade-offs with isotropic structure are observed. It should therefore, be kept in mind, that if similarities between the retrieved isotropic and anisotropic structure are systematically observed, the results could be questionable.
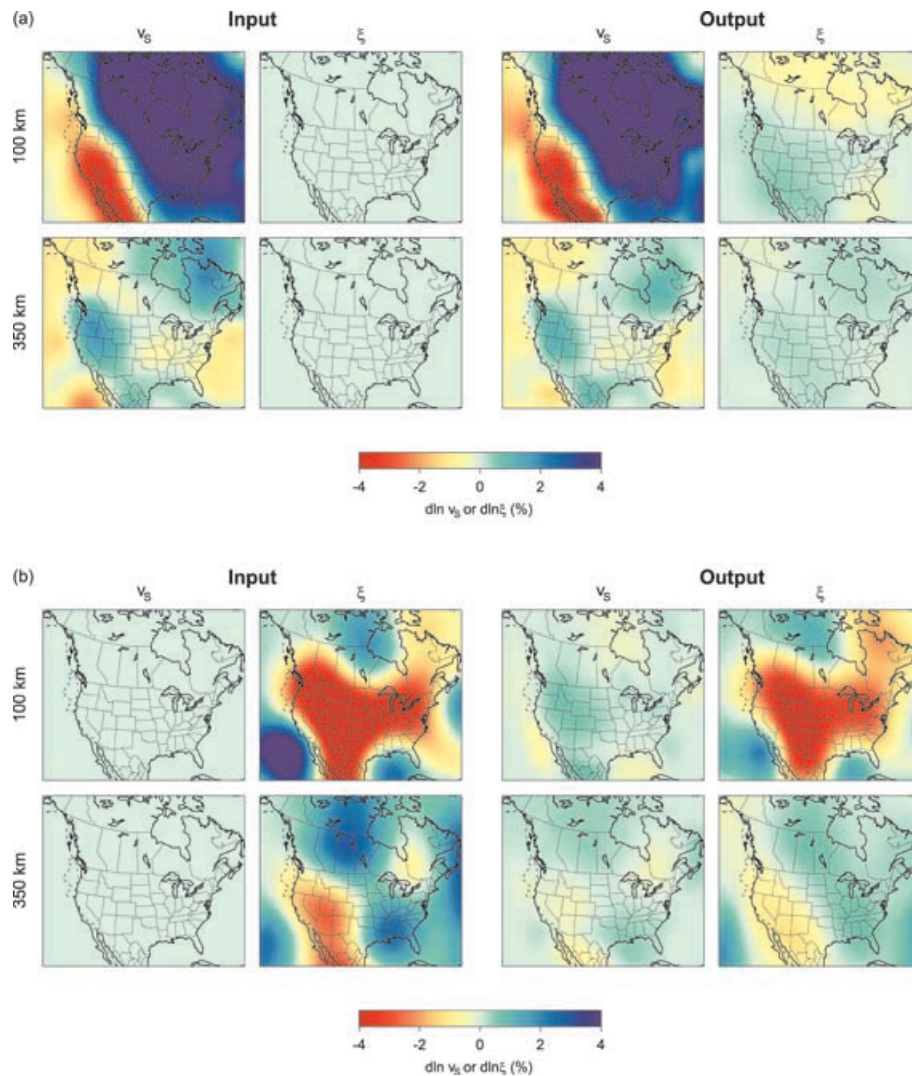
5 RESULTS

5.1 Isotropic *S*-velocity structure

The obtained isotropic *S*-velocity structure for the North American upper mantle is shown in horizontal slices at different depths in Fig. 11. Fig. 13(a) also shows three horizontal slices of the same model but using a different colour scale, which emphasizes different features. This colour scheme allows, in particular, an easy identification of the ±2 per cent contour. Areas characterized by anomalies deviating from the average by less than 1 per cent are left in white, which we assume is the minimum anomaly amplitude we can confidently resolve. Our model confirms large-scale features observed in previous regional traveltime (Grand 1994), dispersion (Godey *et al.* 2004) and waveform studies (e.g. Van der Lee & Nolet 1997a; Frederiksen *et al.* 2001; Van der Lee & Frederiksen 2005), as well as in the used global starting model (Panning & Romanowicz 2006).

With respect to this latter global model, our results are also characterized by shorter-scale features, arising from the finer parametrization adopted, justified by the larger waveform data set used, optimized for resolving the North American upper-mantle structure.

The isotropic *S*-velocity structure of the top part of the upper mantle is controlled by tectonic processes and shows a strong correlation with surface geology. In fact, a striking difference between the low velocity tectonically active western region and the high velocity stable central and eastern shields is observed, with the boundary almost perfectly coincident with the Rocky Mountain Front. This pronounced contrast persists down to 200–250 km depth, where the imaged structure changes character and the large velocity perturbations ($|\delta \ln v_S| > 4$ per cent) observed in the uppermost mantle make way to anomalies of about ±2–3 per cent.

Western North America is characterized by a coast parallel low velocity zone extending as deep as 250 km depth. In the Canadian region, this large negative anomaly is mainly limited to the offshore area, while in the US it penetrates inland, following the Rocky Mountain Front, as far as Idaho, Utah and New Mexico. Most of Northern Mexico is also dominated by this low velocity zone. In the top 100 km, the velocity reduction is as large as 7 per cent, in particular, beneath the US. At 200 km depth it decreases to ≈4 per cent. Deeper, this negative velocity anomaly is limited to the US West coast, while north and south of it, average to high *S*-velocities are imaged. The north–south extent of this feature further decreases with depth and this low velocity anomaly disappears around 300 km depth. The location and shape of this feature agrees fairly well with the results of Van der Lee & Frederiksen (2005), Godey *et al.* (2004) and Frederiksen *et al.* (2001). However, some of these previous models (Van der Lee & Frederiksen 2005) mapped a velocity reduction as large as 9–10 per cent at 100 km depth beneath the Southern Cordillera, California and the Basin and Range, while in our model the maximum negative velocity perturbation at shallow depth is only slightly larger than 7 per cent.

Figure 10. Results for a resolution test addressing trade-offs arising when anomalous structure is present only in the isotropic (a) or anisotropic (b) part of the model. The input model is shown at two different depths on the left half of the page, the isotropic *S*-velocity structure on the left, the radial anisotropic features on the right. The output model is shown on the right half of the page.

Low velocity anomalies are characteristic of recent orogens. Measured high heat flow values, in the range 60–90 mW m^{-2} (e.g. Blackwell & Steele 1992), as well as very low viscosities in the uppermost mantle resolved by geodetic studies (e.g. Bills *et al.* 1994; Kaufmann & Amelung 2000; Nishimura & Thatcher 2003; Pollitz 2003) suggest that the imaged negative velocity perturbations represent young hot asthenospheric material and, consequently, that the lithospheric mantle might be thin or even absent through much of the Western US. These observations are consistent with the slab window hypothesis (Dickinson & Snyder 1979), where hot asthenospheric material flows into the growing gap created by cessation of subduction of the Farallon plate after the oceanic ridge has reached the trench, and consequently heats and weakens the overlying lithosphere. The particularly low *S*-velocities imaged at shallow depths in this region (an average of 4.3 km s^{-1} in the 100–200 km depth range) imply temperatures of approximately 1400° (Cammarano *et al.* 2003), in agreement with the findings of Goes & Van der Lee (2002). These temperatures are not quite high enough to promote partial melting under dry conditions (Thompson 1992). They are, however, high enough to lead to melting if some water is added

(Thompson 1992). In fact, a variety of geochemical and petrological data indicates that vast areas of the uppermost mantle beneath the western US may indeed be anomalously wet (see Dixon *et al.* 2004, for a compilation of studies), possibly as a consequence of dehydration reactions occurred during Laramide subduction of the Farallon plate (Humphreys *et al.* 2003). We therefore suggest that pockets of melt could be present, at least locally, in the western North American uppermost mantle. Presence of melt and/or water in this region is also supported by high upper-mantle electrical conductivities suggested by long-period magnetotelluric investigations (e.g. Egbert & Booker 1992; Lizarralde *et al.* 1995) and recent and ongoing volcanism documented throughout the Cascadian Range.

East of the Rocky Mountain Front, our model shows a large area of fast isotropic *S*-velocities (>2 per cent). This anomaly represents the lithospheric root of the North American craton of Proterozoic and Archean age. If we assume that the 2 per cent contour delimits the base of the craton, we observe the signature of the root as deep as 250 km in correspondence with the oldest part of the continent (Figs 13a and c). The imaged structure suggests that throughout the study region, at 300 km depth, the asthenospheric domain has
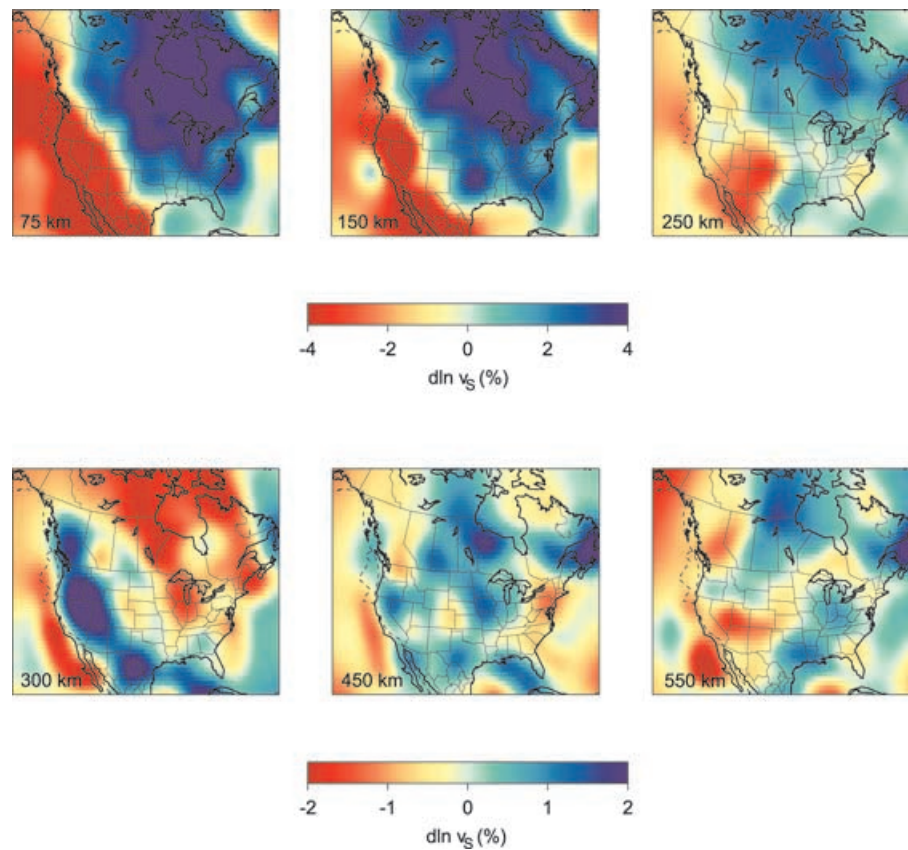
Figure 11. Horizontal slices at different depths through the isotropic *S*-velocity portion of the retrieved tomographic model. Anomalies are relative to the regional average.

been reached. Existing regional *S*-velocity models (Van der Lee & Nolet 1997a; Frederiksen *et al.* 2001; Godey *et al.* 2004; Van der Lee & Frederiksen 2005) show a similar feature. Good agreement is observed, in particular, for the position of the anomaly boundaries.

Deeper than 250–300 km depth, the anomaly amplitudes significantly decrease throughout the study region and heterogeneities in the order of ±2 per cent are imaged. This drastic change in character of the imaged structure with depth is a robust feature and it is not related to the depth dependent resolution of our data set, as confirmed by the resolution tests presented (Figs 5 and 6). The deep upper mantle is characterized by the presence of fast material beneath the western North American coast, replacing low velocity mantle imaged at shallower depth. We relate these positive velocity anomalies to subducted slabs: the Juan de Fuca plate in the north and the extinct Farallon plate in the south.

A band of high seismic velocities, which has been associated with the Farallon plate, is present in the top part of the lower mantle in global *P*- (e.g. Van der Hilst *et al.* 1997) and *S* (Grand 1994) body waves tomographic models, beneath central/eastern North America. Numerical models of mantle convection obtained by imposing the history of Mesozoic–Cenozoic plate motion as a boundary condition (e.g. Bunge & Grand 2000) support the interpretation of this linear positive velocity anomaly as subducted Farallon lithosphere. It is, however, controversial (Severinghaus & Atwater 1990; Schmid *et al.* 2002) whether, in the upper mantle, the subducted Farallon plate is thermally equilibrated with the surrounding mantle, due to the relatively young age of the most recently subducted parts and their high rates of subduction. If thermal equilibration were indeed complete, fragments of Farallon lithosphere should not be distin-

guishable in upper-mantle seismic tomographic models. However, positive seismic velocity anomalies in the deep upper mantle beneath North America have been mapped, in addition to this study (Fig. 11), in previous regional tomographic works (e.g. Romanowicz 1980; Van der Lee & Nolet 1997b). The different techniques and data sets used in these studies further corroborate the robustness of this feature, although details might not agree. The presence of two slab fragments, separated by low velocities associated with the slab window, above 300 km depth, followed by a more continuous high velocity anomaly below, are consistent with tectonic (Severinghaus & Atwater 1990) and kinematic (Schmid *et al.* 2002) models of the subducted Farallon plate. The order of magnitude of the mapped *S*-velocity anomaly is also in agreement with the expected temperature difference between cold subducted lithosphere and the ambient upper mantle (Schmid *et al.* 2002).

5.2 Radial anisotropic structure

The obtained radial anisotropic structure for the North American upper mantle is shown in horizontal slices at different depths in Fig. 12. Anomalies are shown with respect to isotropy. Fig. 13(b) shows the same model, using a different colour scale where the anomalies are relative to anisotropic PREM with the regional average at each depth removed. Our model is characterized by significant anomaly amplitudes, typically larger than the low amplitude artefacts arising from contamination by isotropic *S*-velocity structures in synthetic resolution tests (Fig. 10). Moreover, no one-to-one correspondence (Fig. 10) between the imaged isotropic and anisotropic structure is observed, confirming that the large-scale pattern of the retrieved
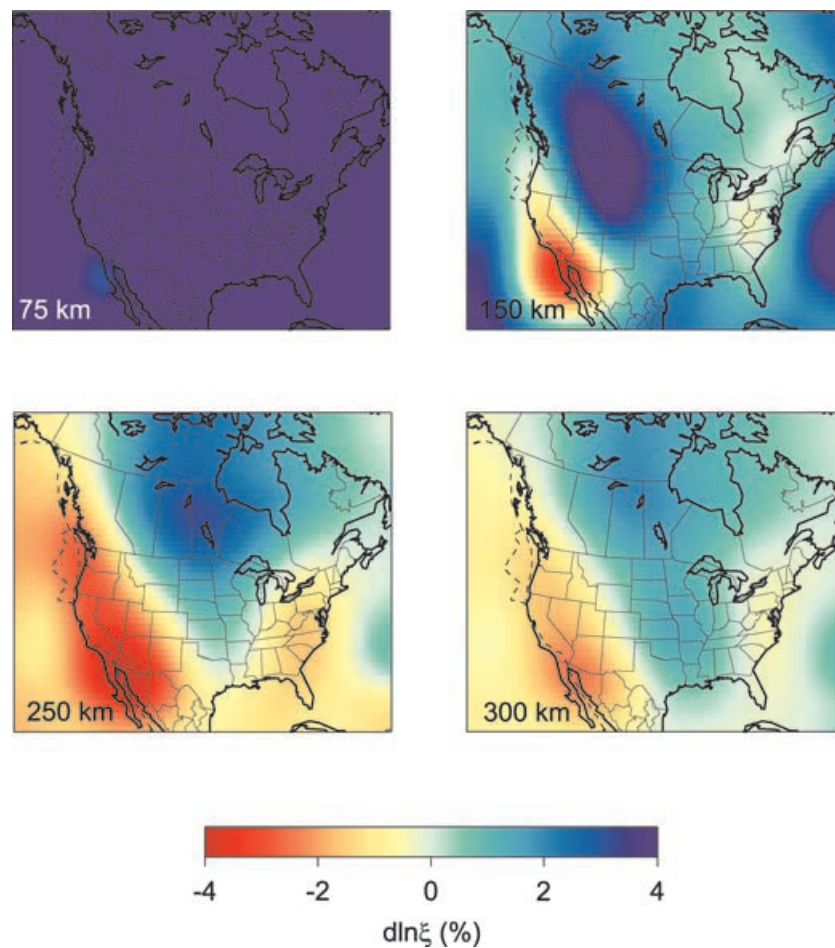
Figure 12. Horizontal slices at different depths through the radial anisotropic portion of the retrieved tomographic model. Anomalies are relative to isotropy.

radial anisotropic structure is resolved and does not originate from trade-offs with the isotropic part of the model.

The shallow part of the North American upper mantle is dominated by a positive ξ anomaly, suggesting horizontally polarized waves travelling faster than vertically polarized waves and, therefore, preferential orientation of the fast axis of anisotropic mantle minerals in the horizontal plane. For instance, at depths shallower than 150 km, a positive anomaly is imaged both beneath the North American continent and the surrounding oceans. The feature mapped in the continental region suggests a lithospheric origin for the observed radial anisotropy, while an asthenospheric contribution is inferred for the oceanic areas, since at these depths, in oceanic environments, asthenospheric conditions dominate. Deeper, this widespread positive ξ anomaly disappears beneath the oceans and its presence is mainly restricted to the cratonic part of the North American continent. At 300 km depth, asthenospheric conditions are present throughout the study region, as suggested by the isotropic S-velocity structure (Figs 11, 13a and c). Persisting radial anisotropy at subcratonic depths (Figs 12, 13b and c) beneath large areas of North America suggests an asthenospheric origin for this feature. The positive sign of this anomaly is consistent with horizontal shear flow in the asthenosphere as the mechanism for the preferred alignment of anisotropic minerals.

The large-scale features characterizing the stable part of the continent are in good agreement with the structure present in the starting model (Panning & Romanowicz 2006).

Presence of radial anisotropy in the asthenosphere beneath the North American cratonic root is also evident from 1-D average profiles. Fig. 14 shows the 1-D isotropic and anisotropic average structure of the stable part of North America (area characterized by $\delta \ln v_S > 2$ per cent at 100 km depth). The average isotropic 1-D S-velocity structure is fairly homogeneous throughout the Archean and Proterozoic part of the continent, with the thickness of the lithosphere varying from 210–250 km in the North to 180–200 km in the South. In contrast, larger variability is observed in the radial anisotropic features between the northern Archean part of the lithospheric root and the southern younger regions, in particular, between 170 and 300 km depth. The shallow portion (down to 170 km depth) of stable North America is characterized by horizontally polarized waves travelling faster than vertically polarized waves, although less radial anisotropy is required by the data than in PREM (Fig. 14). In the older Archean craton, positive ξ anomalies of at least 1 per cent persist down to 300 km, as also observed in horizontal and vertical slices (Figs 13b and c), confirming the presence of both a lithospheric and asthenospheric radial anisotropic layer beneath the cratonic part of the North American continent. A deep positive radial anisotropic anomaly beneath North America, and other cratonic regions, has been previously observed in global tomographic models (Plomerová *et al.* 2002; Gung *et al.* 2003). In particular, the presented anisotropic profiles (Fig. 13c), which suggest the presence of radial anisotropy with $v_{SH} > v_{SV}$ in the depth range 200–350 km, confirm the observations of Gung *et al.* (2003). In the
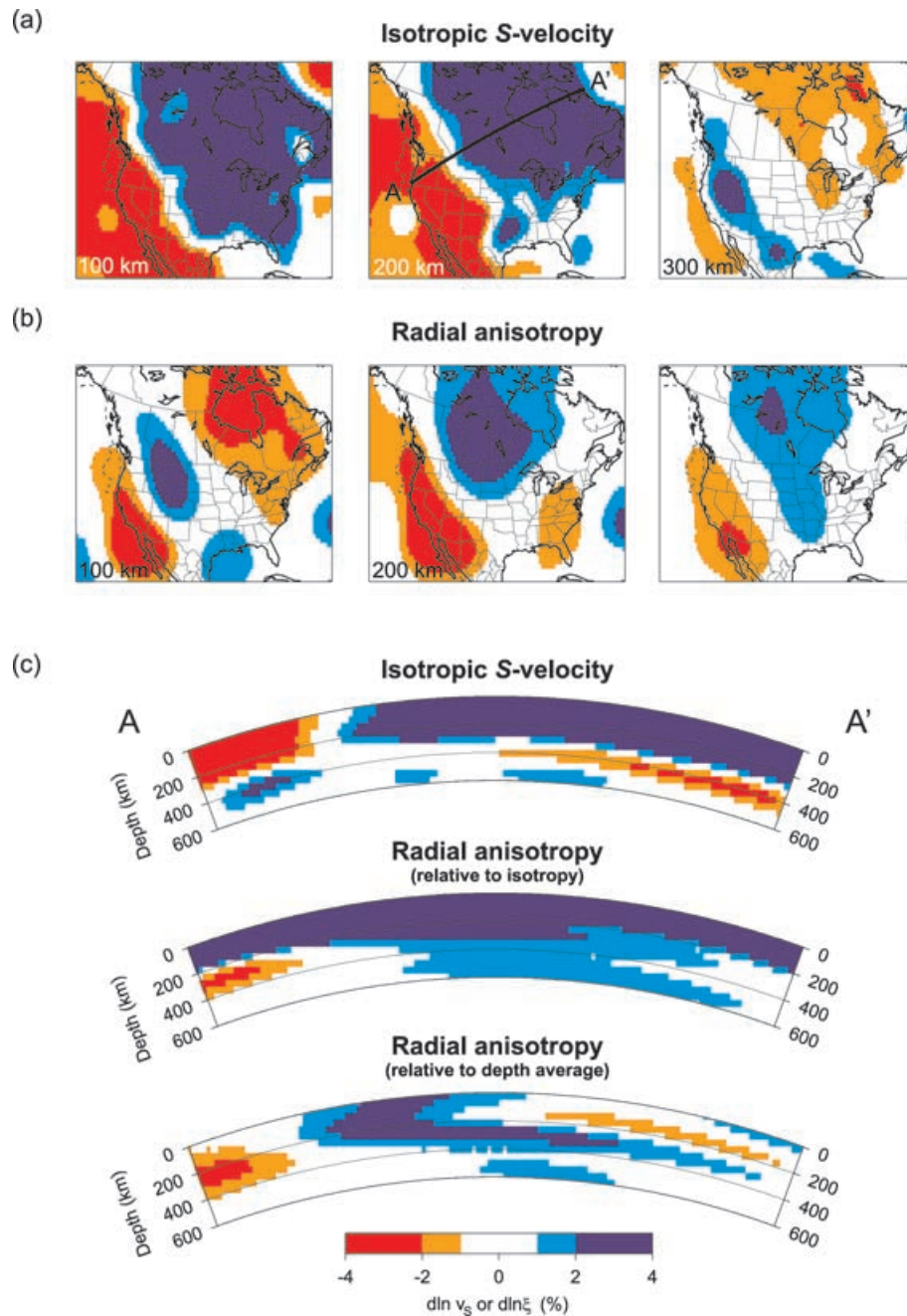
Figure 13. Horizontal (a, b) and vertical (c) slices through the isotropic (a, c) and anisotropic (b,c) portion of the model. Anomalies are with respect to the regional average except for the middle vertical profile, where anomalies are plotted with respect to isotropy. The location of the vertical profiles is shown in the top middle panel.

southern younger regions, the character of radial anisotropy changes towards the base of the lithosphere and a negative anomaly of 1–2 per cent has its maximum at approximately 220 km depth.

In summary, this new regional radial anisotropic model seems to indicate the presence of two distinct anisotropic layers beneath the cratonic part of the North American continent: a deep asthenospheric layer, consistent with present day mantle flow, and a shallower lithospheric layer, possibly a record of ancient tectonic events. These results do not support the view of the lithosphere/asthenosphere boundary being the bottom of an anisotropic upper-mantle region (Karato 1992; Gaherty & Jordan 1995). A

more complete model of anisotropy including both radial and azimuthal anisotropy (Marone & Romanowicz 2007b) confirms that the lithosphere/asthenosphere boundary marks instead a change in the anisotropic features of the mantle (Plomerová *et al.* 2002; Gung *et al.* 2003).

In the tectonically active part of the continent, where the lithosphere is thin, a negative ξ anomaly is mapped deeper than 150 km, in correspondence with the slab window (Fig. 11), suggesting possible mantle upwelling. Although also present in the starting model, at least in Baja California, this feature is stronger and extends more to the north in our retrieved model.
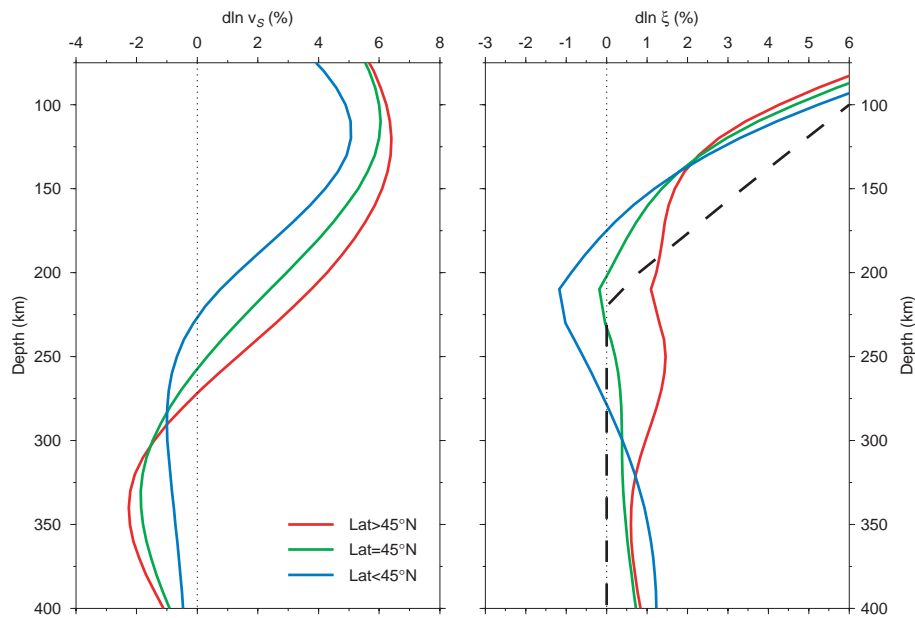
Figure 14. Average 1-D isotropic (left) and anisotropic (right) structures for the stable part of the North American continent. The area considered is defined by $\delta \ln v_S > 2$ per cent at 100 km depth sampled every 5°. Anomalies are with respect to anisotropic PREM for $\delta \ln v_S$ (left), relative to isotropy for $\delta \ln \xi$ (right). The dashed line in the right panel represents the radial anisotropy profile of PREM. For the computation of averages, the area considered has been subdivided according to latitude (colour coding), in order to distinguish the cratonic part of the continent (lat >45°).

6 CONCLUSIONS

Our ultimate goal is a high resolution model for the North American upper mantle including both radial and azimuthal anisotropy. Such a model, characterized by anisotropy with an axis of symmetry of arbitrary orientation, will be within reach with the improved path and azimuthal coverage expected from the USArray data. Here, in a first step, we inverted long period waveform data simultaneously for perturbations in the isotropic S-velocity structure and the anisotropic parameter $\xi = \frac{v_{SH}^2}{v_{SV}^2}$, in the framework of NACT. The resulting 2-D broad-band sensitivity kernels allow us to exploit the information contained in long period seismograms for fundamental and higher mode surface waves at the same time, providing resolution down to the top of the lower mantle.

Our high resolution 3-D radial anisotropic model for the North American upper mantle, derived from more than 45 000 high quality three component fundamental and overtone surface waveforms shares the large-scale features of previous regional studies for North America. In particular, we confirm the pronounced difference in the isotropic velocity structure between the western active tectonic region and the central/eastern stable shield. While the lithosphere is very thin beneath west North America and the oceans surrounding the continent, the imaged high velocity lid reaches a maximum depth of 250 km beneath the oldest part of North America, in agreement with other geophysical data (e.g. Jaupart *et al.* 1998; Rudnick *et al.* 1998). Such lithospheric thickness for the cratonic area is also consistent with global (Gung *et al.* 2003) and regional observations (Debayle & Kennett 2000). These results imply that the presence of a thicker 'tectosphere' (e.g. Jordan 1975) is not required.

The new regional 3-D radial anisotropic model, resolved down to transition zone depths thanks to the inclusion of higher mode waveforms in the NACT framework, indicates the presence of two distinct anisotropic layers beneath the cratonic part of the North American continent: a deep asthenospheric layer, consistent with present day

mantle flow, and a shallower lithospheric layer, possibly a record of ancient tectonic events. This result is confirmed by our subsequent study of azimuthal anisotropy combining surface waveforms and SKS splitting data (Marone & Romanowicz 2007b). These results do not support the view of the lithosphere/asthenosphere boundary as being the bottom of an anisotropic upper-mantle region (Karato 1992; Gaherty & Jordan 1995), but rather, as marking a change in the character of anisotropy as a function of depth, with the anisotropy in the asthenosphere controlled by present day plate motions.

REFERENCES

Aki, K. & Kaminuma, K., 1963. Phase velocity of Love waves in Japan, Part I: Love waves from the Aleutian shock of March 1957, *Bull. Earthq. Res. Inst., Univ. Tokyo*, **41,** 243–259.

Alsina, D., Woodward, R. & Snieder, R., 1996. Shear wave velocity structure in North America from large-scale waveform inversions of surface waves, *J. geophys. Res.*, **101**(B7), 15 969–15 986.

Anderson, D., 1961. Elastic wave propagation in layered anisotropic media, *J. geophys. Res.*, **66,** 2953–2963.

Barruol, G., Silver, P. & Vauchez, A., 1997. Seismic anisotropy in the eastern United States: deep structure of a complex continental plate, *J. geophys. Res.*, **102**(B4), 8329–8348.

Bassin, C., Laske, G. & Masters, G., 2000. The Current Limits of Resolution for Surface Wave Tomography in North America, in *EOS, Trans. Am. geophys. Un.*, Vol. 81, p. F897, Fall Meet. Suppl.

Bills, B., Currey, D. & Marshall, G., 1994. Viscosity estimates for the crust and upper mantle from patterns of lacustrine shoreline deformation in the eastern Great Basin, *J. geophys. Res.*, **99,** 22 059–22 096.

Bird, P., 1988. Formation of the Rocky Mountains, Western United States: a Continuum Computer Model, *Science*, **239,** 1501–1507.

Blackwell, D. & Steele, J., 1992. *Geothermal Map of North America*, scale 1:5,000,000, Geol. Soc. Am., Boulder, Colo.

Boschi, L. & Ekström, G., 2002. New images of the Earth's upper mantle from measurements of surface wave phase velocity anomalies, *J. geophys. Res.*, **107**(B4), doi:10.1029/2000JB000059.

Boschi, L., Ekström, G. & Kustowski, B., 2004. Multiple resolution surface wave tomography, the Mediterranean Basin, *Geophys. J. Int.*, **157,** 293–304.

Bostock, M. & Cassidy, J., 1995. Variations in *SKS* splitting across western Canada, *Geophys. Res. Lett.*, **22**(1), 5–8.

Bunge, H.-P. & Grand, S., 2000. Mesozoic plate-motion history below the northeast Pacific Ocean from seismic images of the subducted Farallon slab, *Nature*, **405,** 337–340.

Cammarano, F., Goes, S., Vacher, P. & Giardini, D., 2003. Inferring upper mantle temperatures from seismic velocities, *Phys. Earth planet. Inter.*, **138,** 197–222.

Cara, M. & Lévêque, J., 1988. Anisotropy of the asthenosphere: the higher mode data of the Pacific revisited, *Geophys. Res. Lett.*, **15**(3), 205–208.

Debayle, E. & Kennett, B., 2000. Anisotropy in the Australasian upper mantle from Love and Rayleigh waveform inversion, *Earth planet. Sci. Lett.*, **184,** 339–351.

Debayle, E., Kennett, B. & Priestley, K., 2005. Global azimuthal seismic anisotropy and the unique plate-motion deformation of Australia, *Science*, **433,** 509–512.

Dickinson, W. & Snyder, W., 1979. Geometry of subducted slabs related to San Andreas transform, *J. Geol.*, **87,** 609–627.

Dixon, J., Dixon, T., Bell, D. & Malservisi, R., 2004. Lateral variation in upper mantle viscosity: role of water, *Earth planet. Sci. Lett.*, **222,** 451–467.

Dziewonski, A. & Anderson, D., 1981. Preliminary reference Earth model, *Phys. Earth planet. Inter.*, **25,** 297–356.

Egbert, G. & Booker, J., 1992. Very long period magnetotellurics at Tucson Observatory: implications for mantle conductivity, *J. geophys. Res.*, **97**(B11), 15 099–15 112.

Ekström, G. & Dziewonski, A., 1998. The unique anisotropy of the Pacific upper mantle, *Nature*, **394,** 168–172.

Estey, L. & Douglas, B., 1986. Upper mantle anisotropy: a preliminary model, *J. geophys. Res.*, **91,** 11 393–11 406.

Fouch, M., Fischer, K., Parmentier, E., Wysession, M. & Clarke, T., 2000. Shear wave splitting, continental keels, and patterns of mantle flow, *J. geophys. Res.*, **105**(B3), 6255–6275.

Frederiksen, A., Bostock, M. & Cassidy, J., 2001. S-wave velocity structure of the Canadian upper mantle, *Phys. Earth planet. Inter.*, **124,** 175–191.

Gaherty, J., 2004. A surface wave analysis of seismic anisotropy beneath eastern North America, *Geophys. J. Int.*, **158,** 1053–1066.

Gaherty, J. & Jordan, T., 1995. Lehmann Discontinuity as the Base of an Anisotropic Layer Beneath Continents, *Science*, **268,** 1468–1471.

Godey, S., Snieder, R., Villaseñor, A. & Benz, H., 2003. Surface wave tomography of North America and the Caribbean using global and regional broad-band networks: phase velocity maps and limitations of ray theory, *Geophys. J. Int.*, **152,** 620–632.

Godey, S., Deschamps, F., Trampert, J. & Snieder, R., 2004. Thermal and compositional anomalies beneath the North American continent, *J. geophys. Res.*, **109,** doi:10.1029/2002JB002263.

Goes, S. & Van der Lee, S., 2002. Thermal structure of the North American uppermost mantle inferred from seismic tomography, *J. geophys. Res.*, **107,** doi:10.1029/2000JB000049.

Grand, S., 1994. Mantle shear structure beneath the Americas and surrounding oceans, *J. geophys. Res.*, **99,** 591–621.

Gung, Y., Panning, M. & Romanowicz, B., 2003. Global anisotropy and the thickness of continents, *Nature*, **422,** 707–711.

Humphreys, E., Hessler, E., Dueker, K., Lang Farmer, G., Erslev, E. & Atwater, T., 2003. How Laramide-age hydration of North American lithosphere by the Farallon slab controlled subsequent activity in the western US, *Int. Geol. Rev.*, **45,** 575–595.

Jaupart, C., Mareschal, J. & Guillou-Frottier, L., 1998. Heat flow and thickness of the lithosphere in the Canadian Shield, *J. geophys. Res.*, **103,** 15 269–15 286.

Jordan, T., 1975. Continental Tectosphere, *Rev. Geoph.*, **13**(3), 1–12.

Karato, S., 1992. On the Lehmann discontinuity, *Geophys. Res. Lett.*, **19**(22), 2255–2258.

Kaufmann, G. & Amelung, F., 2000. Reservoir-induced deformation and continental rheology in vicinity of Lake Mead, Nevada, *J. geophys. Res.*, **105,** 16 341–16 358.

Kay, I., Sol, S., Kendall, J.-M., Thomson, C., White, D., Asudeh, I., Roberts, B. & Francis, D., 1999. Shear wave splitting observations in the Archean craton of Western Superior, *Geophys. Res. Lett.*, **26**(17), 2669–2672.

Lancaster, P. & Salkauskas, K., 1986. *Curve and Surface Fitting, an Introduction*, Academic Press, London.

Lévêque, J. & Cara, M., 1983. Long-period Love wave overtone data in North America and the Pacific Ocean: new evidence for upper mantle anisotropy, *Phys. Earth planet. Inter.*, **33,** 164–179.

Lévêque, J. & Cara, M., 1985. Inversion of multimode surface wave data: evidence for sub-lithospheric anisotropy, *Geophys. J. R. astr. Soc.*, **83,** 753–773.

Levin, V., Menke, W. & Park, J., 1999. Shear wave splitting in the Appalachians and the Urals: a case for multilayered anisotropy, *J. geophys. Res.*, **104**(B8), 17 975–17 993.

Li, A., Forsyth, D. & Fischer, K., 2003. Shear velocity structure and azimuthal anisotropy beneath eastern North America from Rayleigh wave inversion, *J. geophys. Res.*, **108**(B8), doi:10.1029/2002JB002259.

Li, A., Forsyth, D. & Fischer, K., 2005. Rayleigh wave phase velocities and azimuthally anisotropic shear-wave structure beneath the Colorado Rocky Mountains, in *The Rocky Mountain Region—An Evolving Lithosphere: Tectonics, Geochemistry, and Geophysics*, eds Karlstrom, K. & Keller, G., pp. 385–401, Geophysical Monograph Series 154, American Geophysical Union.

Li, X. & Romanowicz, B., 1995. Comparison of global waveform inversions with and without considering cross branch coupling, *Geophys. J. Int.*, **121,** 695–709.

Li, X. & Romanowicz, B., 1996. Global mantle shear velocity model developed using nonlinear asymptotic coupling theory, *J. geophys. Res.*, **101,** 22 245–22 273.

Liu, H., Davis, M. & Gao, S., 1995. *SKS* splitting beneath southern California, *Geophys. Res. Lett.*, **22**(7), 767–770.

Lizarralde, D., Chave, A., Hirth, G. & Schultz, A., 1995. Northeastern Pacific mantle conductivity profile from long-period magnetotelluric sounding using Hawaii-to-California submarine cable data, *J. geophys. Res.*, **100**(B9), 17 837–17 854.

Love, A., 1927. *A Treatise on the Mathematical Theory of Elasticity*, Cambridge University Press, Cambridge.

Marone, F. & Romanowicz, B., 2007a. Non-linear crustal corrections in high resolution regional waveform seismic tomography, *Geophys. J. Int.*, in press.

Marone, F. & Romanowicz, B., 2007b. The depth distribution of azimuthal anisotropy in the continental upper mantle, *Nature*, **447,** 198–201.

McEvilly, T., 1964. Central U.S. crust-upper mantle structure from Love and Rayleigh wave phase velocity inversion, *Bull. seism. Soc. Am.*, **54,** 1997–2015.

Mégnin, C. & Romanowicz, B., 2000. The 3D shear velocity structure of the mantle from the inversion of body, surface and higher mode waveforms, *Geophys. J. Int.*, **143,** 709–728.

Menke, W., 1989. *Geophysical Data Analysis: Discrete Inverse Theory*, (revised edition) Academic, San Diego.

Montagner, J.-P. & Anderson, D., 1989. Petrological constraints on seismic anisotropy, *Phys. Earth planet. Inter.*, **54,** 82–105.

Montagner, J.-P. & Jobert, N., 1988. Vectorial tomography; II. Application to the Indian Ocean, *Geophys. J.*, **94,** 309–344.

Montagner, J.-P. & Nataf, H.-C., 1988. Vectorial tomography; I. Theory, *Geophys. J.*, **94,** 295–307.

Montagner, J.-P. & Tanimoto, T., 1991. Global upper mantle tomography of seismic velocities and anisotropies, *J. geophys. Res.*, **96,** 20 337–20 351.

Nataf, H.-C., Nakanishi, I. & Anderson, D., 1984. Anisotropy and shear-velocity heterogeneities in the upper mantle, *Geophys. Res. Lett.*, **11,** 109–112.

Nataf, H.-C., Nakanishi, I. & Anderson, D., 1986. Measurements of mantle wave velocities and inversion for lateral heterogeneities and anisotropy; 3. Inversion, *J. geophys. Res.*, **91,** 7261–7307.

National Geophysical Data Center, 1988. ETOPO-5, bathymetry/topography data, Data Announc. *88-MGG-02, Natl. Oceanic and Atmos. Admin., U.S. Dep. of Commer.*, Washington, DC.

Nishimura, T. & Thatcher, W., 2003. Rheology of the lithosphere inferred from post-seismic uplift following the 1959 Hebgen Lake earthquake, *J. geophys. Res.*, **108**(B8), 2389, doi:10.1029/2002JB002191.

Özalaybey, S. & Savage, M., 1995. Shear-wave splitting beneath western United States in relation to plate tectonics, *J. geophys. Res.*, **100**(B9), 18 135–18 149.

Panning, M. & Romanowicz, B., 2004. Inferences on flow at the base of Earth's mantle based on seismic anisotropy, *Science*, **303,** 351–353.

Panning, M. & Romanowicz, B., 2006. A three dimensional radially anisotropic model of shear velocity in the whole mantle, *Geophys. J. Int.*, **167**(1), 361–379.

Plomerová, J., Kouba, D. & Babuška, V., 2002. Mapping the lithosphere-asthenosphere boundary through changes in surface-wave anisotropy, *Tectonophysics*, **358,** 175–185.

Pollitz, F., 2003. Transient rheology of the uppermost mantle beneath the Mojave Desert, California, *Earth planet. Sci. Lett.*, **215,** 89–104.

Romanowicz, B., 1980. Large scale three dimensional *P* velocity structure beneath the western U.S. and the lost Farallon plate, *Geophys. Res. Lett.*, **7**(5), 345–348.

Romanowicz, B., 1987. Multiplet-multiplet coupling due to lateral heterogeneity: asymptotic effects on the amplitude and frequency of the Earth's normal modes, *Geophys. J. R. astr. Soc.*, **90**(1), 75–100.

Romanowicz, B., Gung, Y., Panning, M., Lekic, V. & Capdeville, Y., 2007. *Computation of seismograms in a 3D earth: various levels of approximation and their contributions*, in preparation.

Rudnick, R., McDonough, W. & O'Connell, R., 1998. Thermal structure, thickness and composition of continental lithosphere, *Chem. Geol.*, **145,** 395–411.

Savage, M. & Sheehan, A., 2000. Seismic anisotropy and mantle flow from the Great Basin to the Great Plains, western United States, *J. geophys. Res.*, **105**(17), 13 715–13 734.

Savage, M. & Silver, P., 1993. Mantle deformation and tectonics: constraints from seismic anisotropy in the western United States, *Phys. Earth planet. Inter.*, **78,** 207–227.

Savage, M., Silver, P. & Meyer, R., 1990. Observations of teleseismic shear-wave splitting in the Basin and Range from portable and permanent stations, *Geophys. Res. Lett.*, **17**(1), 21–24.

Savage, M., Sheehan, A. & Lerner-Lam, A., 1996. Shear wave splitting across the Rocky Mountain Front, *Geophys. Res. Lett.*, **23**(17), 2267–2270.

Schmid, C., Goes, S., Van der Lee, S. & Giardini, D., 2002. Fate of the Cenozoic Farallon slab from a comparison of kinematic thermal modeling with tomographic images, *Earth planet. Sci. Lett.*, **204,** 17–32.

Severinghaus, J. & Atwater, T., 1990. Cenozoic geometry and thermal state of the subducting slabs beneath western North America, in *Basin and Range Extensional Tectonics Near the Latitude of Las Vegas, Nevada*, ed. Wernicke, B., pp. 1–22, Geological Society of America Memoir 176, Boulder, Colorado.

Silver, P. & Chan, W., 1988. Implications for continental structure and evolution from seismic anisotropy, *Nature*, **335,** 34–39.

Silver, P. & Kaneshima, S., 1993. Constraints on mantle anisotropy beneath Precambrian North America from a transportable teleseismic experiment, *Geophys. Res. Lett.*, **20**(12), 1127–1130.

Tanimoto, T. & Anderson, D., 1984. Mapping convection in the mantle, *Geophys. Res. Lett.*, **11,** 287–290.

Tarantola, A., 2004. *Inverse Problem Theory and Methods for Model Parameter Estimation*, Society of Industrial and Applied Mathematics.

Tarantola, A. & Valette, B., 1982. Generalized nonlinear inverse problems solved using the least squares criterion, *Rev. Geophys. Space Phys.*, **20,** 219–232.

Thompson, A., 1992. Water in the Earth's upper mantle, *Nature*, **358,** 295–302.

Van der Hilst, R., Widiyantoro, S. & Engdahl, E., 1997. Evidence for deep mantle circulation from global tomography, *Nature*, **386**(6625), 578–584.

Van der Lee, S., 2002. High-resolution estimates of lithosphere thickness from Missouri to Massachusetts, USA, *Earth planet. Sci. Lett.*, **203,** 15–23.

Van der Lee, S. & Frederiksen, A., 2005. Surface Wave Tomography applied to the North American Upper Mantle, in *Seismic Earth: Array Analysis of Broadband Seismograms*, eds Nolet, G. & Levander, A., pp. 67–80, Geophysical Monograph Series 157, American Geophysical Union.

Van der Lee, S. & Nolet, G., 1997a. Upper mantle *S*-velocity structure of North America, *J. geophys. Res.*, **102,** 22 815–22 838.

Van der Lee, S. & Nolet, G., 1997b. Seismic image of the subducted trailing fragments of the Farallon plate, *Nature*, **386,** 266–269.

Vinnik, L., Makeyeva, L., Milev, A. & Usenko, A., 1992. Global patterns of azimuthal anisotropy and deformations in the continental mantle, *Geophys. J. Int.*, **111,** 433–447.

Wang, Z. & Dahlen, F., 1995. Validity of surface-wave ray theory on a laterally heterogeneous Earth, *Geophys. J. Int.*, **123**(3), 757–773.

Wang, Z., Tromp, J. & Ekström, G., 1998. Global and regional surface-wave inversions: a spherical-spline parameterization, *Geophys. Res. Lett.*, **25**(2), 207–210.

Wilson, D. *et al.*, 2002. Broadband seismic background noise at temporary seismic stations observed on a regional scale in the Southwestern United States, *Bull. seism. Soc. Am.*, **92**(8), 3335–3341.

Wilson, D., Aster, R. & the, RISTRA Team, 2003. Imaging crust and upper mantle seismic structure in the Southwestern United States using teleseismic receiver functions, *The Leading Edge*, **22**(3), 232–237.

Woodhouse, J. & Dziewonski, A., 1984. Mapping the upper mantle: three dimensional modeling of earth structure by inversion of seismic waveforms, *J. geophys. Res.*, **89,** 5953–5986.

Wysession, M., Fischer, K., Clarke, T., Al-Eqabi, G., Fouch, M., Shore, P., Valenzuela, R., Li, A. & Zaslow, M., 1996. Slicing into the Earth, *EOS, Trans. Am. geophys. Un.*, **77**(48), 477–482.

Zhou, Y., Dahlen, F., Nolet, G. & Laske, G., 2005. Finite-frequency effects in global surface-wave tomography, *Geophys. J. Int.*, **163,** 1087–1111.